*Geophys. J. Int.* (2009) **176,** 353–367 doi: 10.1111/j.1365-246X.2008.03932.x



# The postseismic response to the 2002 *M* 7.9 Denali Fault earthquake: constraints from InSAR 2003–2005

Juliet Biggs,[1,*] Roland Burgmann,[2] Jeffrey T. Freymueller,[3] Zhong Lu,[4] Barry Parsons,[1] Isabelle Ryder,[2] Gina Schmalzle[5] and Tim Wright[6]

[1] *COMET, Department of Earth Sciences, University of Oxford, Parks Road, Oxford,* OX1 3PR*, UK. E-mail: Juliet.Biggs@earth.ox.ac.uk*
[2] *University of California, Berkeley, USA*
[3] *Geophysical Institute, University of Alaska, Fairbanks, AK, USA*
[4] *USGS, Cascades Volcano Observatory, Vancouver, WA, USA*
[5] *Rosenstiel School of Marine and Atmospheric Sciences, University of Miami, FL, USA*
[6] *School of Earth and Environment, University of Leeds, Leeds, UK*

Accepted 2008 August 7. Received 2008 July 26; in original form 2008 February 11

## SUMMARY

InSAR is particularly sensitive to vertical displacements, which can be important in distinguishing between mechanisms responsible for the postseismic response to large earthquakes (afterslip, viscoelastic relaxation). We produce maps of the surface displacements resulting from the postseismic response to the 2002 Denali Fault earthquake, using data from the Canadian Radarsat-1 satellite from the periods summer 2003, summer 2004 and summer 2005. A peak-to-trough signal of amplitude 4 cm in the satellite line of sight was observed between summer 2003 and summer 2004. By the period between summer 2004 and summer 2005, the displacement rate had dropped below the threshold required for observation with InSAR over a single year. The InSAR observations show that the principal postseismic relaxation process acted at a depth of ∼50 km, equivalent to the top of the mantle. However, the observations are still incapable of distinguishing between distributed (viscoelastic relaxation) and localized (afterslip) deformation. The imposed coseismic stresses are highest in the lower crust and, assuming a Maxwell rheology, a viscosity ratio of at least 5 between lower crust and upper mantle is required to explain the contrast in behaviour. The lowest misfits are produced by mixed models of viscoelastic relaxation in the mantle and shallow afterslip in the upper crust. Profiles perpendicular to the fault show significant asymmetry, which is consistent with differences in rheological structure across the fault.

**Key words:** Space geodetic surveys; Seismic cycle; Radar interferometry; Continental tectonics: strike-slip and transform; Rheology: crust and lithosphere.

## 1 INTRODUCTION

Postseismic deformation is the transient response of the lithosphere to the sudden change of stresses caused by an earthquake. Observations show that displacements are typically an order of magnitude smaller than coseismic displacements and decay with longer spatial wavelengths and that the rate of displacement decreases with time over a period of years following the earthquake. A number of mechanisms have been proposed to explain this response, including afterslip on a discrete fault plane (e.g. Bürgmann *et al.* 2002), creep in a viscous or viscoelastic shear zone (e.g. Hearn *et al.* 2002), viscoelastic relaxation in the lower crust/upper mantle (e.g. Pollitz *et al.* 2000) and poroelastic rebound (e.g. Jonsson *et al.* 2003).

To investigate the causal mechanism behind the postseismic transient, it is necessary to observe surface displacements with good spatial and temporal resolution over time periods ranging from days to decades following the earthquake. Triangulation and levelling surveys offer measurements of long-term postseismic response from historic earthquakes such as the 1906 San Francisco earthquake (e.g. Kenner & Segall 2000). For such historic earthquakes, space geodetic techniques such as InSAR and Global Positioning System (GPS) offer the opportunity to measure late-stage postseismic transients (Gourmelen & Amelung 2005), and for more recent earthquakes, they can be used to measure the early phase of postseismic response in greater temporal and spatial detail. Only a small number of continental earthquakes of sufficient magnitude (*M* 7+) have occurred since regular SAR acquisitions began. Those

*Now at: Rosenstiel School of Marine and Atmospheric Sciences, University of Miami, FL, USA.

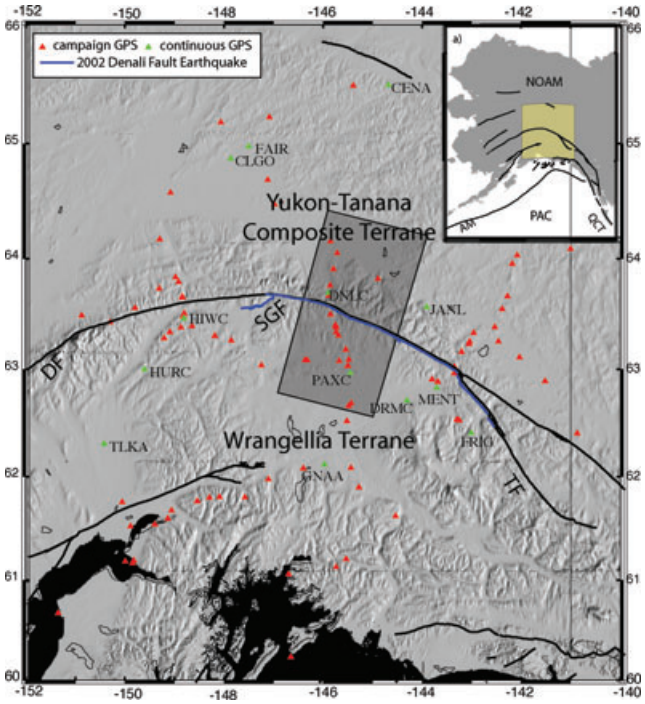


**Figure 1.** Location of the 2002 Denali Fault earthquake rupture (blue line). Continuous GPS stations are shown in green, campaign GPS stations in red. Radarsat track used in this study is shown as a grey box. DF—Denali Fault; TF—Totschunda Fault; SGF—Susitna Glacier Fault. Inset: NOAM—North American Plate; PAC—Pacific Plate; QCT—Queen Charlotte Transform; AM—Aleutian Megathrust.

examples that have been studied occur in arid conditions with good coherence [Manyi, Tibet, (Ryder *et al.* 2007); Landers, California (Fialko 2004); Hector Mine, California (Jacobs *et al.* 1999; Pollitz *et al.* 2001)].

The $M_w$ 7.9 Denali Fault (DF) earthquake in 2002 was the largest continental strike-slip earthquake in North America since the 1857 Fort Tejon, California event and provides a new opportunity to study postseismic deformation using InSAR (Fig. 1). The earthquake initiated as a thrust event on the previously unrecognized Susitna Glacier Fault (SGF) and propagated eastwards, transferring onto the right-lateral DF, which ruptured for a distance of ∼200 km, before finally rupturing the Totschunda Fault for a distance of ∼70 km. The total rupture length was 340 km with surface offsets of up to 9 m (Eberhart-Phillips *et al.* 2003).

### 1.1 Tectonic background

The tectonics of Alaska are controlled by the interaction between the Pacific and North American plates, forming one of the most seismically active areas in the world (Fig. 1). Both the rate of convergence and the nature of the interface changes along the plate boundary. In the west, the Pacific Plate is subducting under the North American Plate at a rate of 68 mm yr$^{-1}$, along the Aleutian Megathrust. To the east, the Queen Charlotte Transform is a transpressive, strike-slip fault. On both, the relative motion is taken up in an 'oceanic plate style', that is, a single earthquake mechanism dominates within a very narrow zone of deformation. Linking these two contrasting styles of plate boundary is a complex region of continental deformation extending several hundred kilometres inland through southern Alaska (Fig. 1). The DF, cutting through the Alaska Range, is a major geomorphological feature, extending for over a thousand kilometres. Estimates of the slip rate on the DF are variable (Biggs *et al.* 2007), ranging from ≤3 to 10–20 mm yr$^{-1}$. Recent geodetic estimates include 10.5 ± 5 mm yr$^{-1}$ from InSAR (Biggs *et al.* 2007) and 8 ± 5 mm yr$^{-1}$ from GPS (Fletcher 2002). By dating boulders and sediments from offset moraines, Matmon *et al.* (2006) find a decrease in slip rate from east (14.4 ± 2.5 mm yr$^{-1}$) to west (9.4 ± 1.6 mm yr$^{-1}$) along the DF.

### 1.2 GPS observations and models

The DF earthquake occurred within a pre-existing network of campaign GPS sites which have been compared to interseismic models (Fletcher 2002). Within 2 weeks of the earthquake, 10 new continuous GPS (cGPS) sites were installed, and an additional five sites were added the following summer. Between 2002 and 2005, six measurement campaigns took place at about 100 sites in the area, with observational durations of 48–72 hr. The GPS sites provide excellent constraints on the time-dependence of the postseismic transient (Pollitz 2005; Freed *et al.* 2006b), with measurements showing horizontal velocities of up to 300 mm yr$^{-1}$ in the first 0.1 yr and up to 100 mm yr$^{-1}$ for the next 1.5 yr (Pollitz 2005). Previous studies (Pollitz 2005; Freed *et al.* 2006a,b) agree that non-linear viscoelastic deformation in the upper mantle is key to explaining the observed postseismic transients at far-field sites, but an additional contribution from shallow afterslip and/or poroelastic rebound is required to match near-field observations. Johnson *et al.* (2008) show that the first 4 yr of GPS observations can be matched using a coupled model of afterslip on the fault in the lithosphere and distributed viscous flow in the asthenosphere. The ability of GPS studies to distinguish between postseismic mechanisms and determine the rheological structure, is limited by the sparsity of GPS sites and lack of precision on the vertical component of displacement. InSAR has the potential to resolve these issues.

## 2 GEODETIC DATA

### 2.1 InSAR

We use radar data collected by the Canadian Radarsat-1 satellite during the period 2003–2005 and archived by the Alaska Satellite Facility (Table S1). We focus on the area of the rupture, which coseismic (Wright *et al.* 2004) and interseismic studies (Biggs *et al.* 2006) have shown to have good interferometric coherence (Fig. 1). The DF earthquake occurred in 2002 November, but since snow cover makes winter acquisitions unusable, the first date that can be used to make postseismic interferograms is 2003 July. Similarly, acquisitions during the periods 2003 November to 2004 June and 2004 September to 2005 June cannot be used to make interferograms, leaving gaps in the time-series. Of the interferograms processed, 41 descending, interconnected image pairs showed sufficient coherence for further study. The interferograms were processed using the GAMMA software, filtered using a power-spectrum filter (Goldstein & Werner 1998), unwrapped using a minimum cost flow algorithm (Chen & Zebker 2000) and multilooked to a pixel size of 4 km.

### 2.2 GPS

Although this paper is primarily concerned with the analysis and modelling of InSAR data, combining the InSAR with GPS

measurements has several advantages. In particular, combining line-of-sight InSAR measurements with horizontal GPS vectors can give us a direct estimate of the vertical component of motion, and GPS measurements of far-field displacements can be used to stabilize afterslip inversions, in which the InSAR data only cover part of the rupture. To facilitate this, we reprocess existing GPS data, from both campaign and continuous sites, to calculate the displacements over a similar time period to our InSAR observations.

GPS site displacements were estimated from a time-series of site positions, with each daily solution analysed independently, using a strategy similar to that of Freymueller *et al.* (2000). Surveys of campaign GPS sites in the summers of 2003 and 2004 extended over a period of 5–6 months, with some sites being surveyed twice each year and others only once. To include as many sites as possible, we estimated the displacements by fitting a velocity to all data from 2003 May to 2004 October, and using the annual rate as the 1-yr displacement. We estimated velocities in the ITRF2000 reference frame of the GPS time-series, and subtracted the motion of North America to give a North America-fixed frame, that is, the closest approximation for the InSAR frame with a ramp removed. Although the averaging time for the GPS data is slightly different from that of the InSAR data, the two data sets record substantially the same signal.

## 3 INSAR ANALYSIS

### 3.1 Stacking

A preliminary analysis is carried out by selecting the most coherent interferograms, correcting them individually for their orbital errors and stacking them. Four interferograms for the interval from summer 2003 to summer 2004 were chosen (030714–040708, 030807–040708, 030831–040708, 030924–040708; date format is yymmdd), equivalent to a total duration of 3.55 yr. All four interferograms have a common radar image (04 07 08), so the stack will be significantly biased by orbital and/or atmospheric contributions on this day.

To provide a first-order correction to the orbital errors, regions in which deformation was expected to be small were selected (far-field regions more than ∼70 km from the fault and areas close to the fault), and the best-fitting quadratic polynomial to these areas was removed from each interferogram. The interferograms were then summed at all pixels which were commonly coherent, and a further quadratic polynomial removed from the stack. The resulting stack, and profile perpendicular to the fault, is shown in Fig. 2.

Although the techniques used to produce this stack are not rigorous, the resulting image is consistent with models of the postseismic deformation, based on the horizontal displacements observed by GPS. To the north of the fault, there is a clear peak in displacement at a distance of 50-60 km from the fault, consistent with deformation at depths of 50–60 km, that is, the upper mantle. To the south of the fault, the peak displacement is more distributed and occurs over distances 10–70 km from the fault.

### 3.2 Network approach

By choosing only the most coherent interferograms, and only analysing pixels which are always coherent, large quantities of useful data are abandoned. In a more complete approach, we use a network of 41 interferograms from 14 radar images (Supporting Information) to analyse the displacement field, using all interferograms which are coherent at varying numbers of pixels. By using an appropriate variance–covariance matrix (Biggs *et al.* 2007), the bias introduced by using interferograms with common images is reduced. Instead of applying an orbital correction to each interferogram, the complete network is used to estimate the orbital error on each radar image.

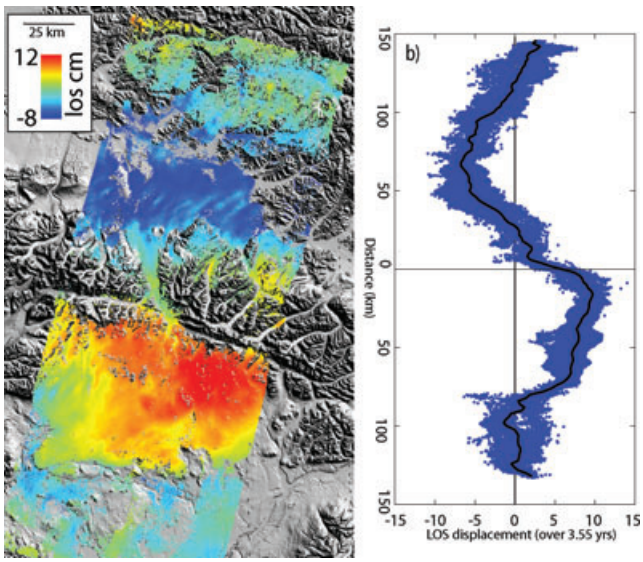


**Figure 2.** (a) Stack of four interferograms from the time period summer 2003–summer 2004. Total duration is 3.55 yr, giving a peak range change of ∼2– 3 cm in the satellite line-of-sight over a 1-yr time period. (b) Profile taken perpendicular to the fault. Peak displacement is located ∼50–60 km from the fault in the north. Profile values are taken from the entire image and the black line is a bin average.

The minimum cost flow algorithm, while allowing an objective way of unwrapping interferograms with low coherence, introduces a significant number of unwrapping errors due to the assumption that the phase gradient is small. While this assumption is valid for the postseismic signal, the errors in the orbital parameters of Radarsat cause a significant phase gradient. To reduce this, two unwrapping steps are performed; the first is a preliminary attempt which allows a network orbital correction to be performed on the interferograms. Based on this, quadratic polynomials approximating the orbital error on each acquisition are removed from the wrapped interferograms, and a second unwrapping procedure is carried out. The parameters of the estimated surfaces appear random in time, consistent with our assumption that the quadratic functional form fits the orbital rather than deformation component of the interferograms (Supporting Information).

Once the interferograms are unwrapped and the orbital errors corrected, they are resampled to 4 km pixel spacing to reduce the number of data points for inversion. Given that the acquisition dates are clustered around the summer months, a full time-series approach is not warranted. Instead, the interferograms are divided into two groups—2003–2004 (28 interferograms) and 2004–2005 (16 interferograms). Four interferograms which are created using images only from 2004 are included in both groups. The best-fitting rate (in mm yr$^{-1}$) in each time period, $\mathbf{r}_{\rm los}$, is found using a least-squares matrix inversion on a pixel-by-pixel basis,

$$\frac{2\pi}{\lambda}\mathbf{T}\,\mathbf{r}_{\rm los} = \mathbf{P}, \qquad (1)$$

where $\lambda$ is the radar wavelength in mm and $\mathbf{P} = [\phi_{12}, \phi_{23}, \phi_{34} \ldots \phi_{mn}]^T$ is a vector containing the phase for each

interferogram which is coherent at that pixel. **T** is a matrix containing the time-spans, $t_{mn}$, of the relevant interferograms. For example, if interferograms $i_{12}$ and $i_{23}$ are within the first time period and interferogram $i_{45}$ is within the second time period, then,

$$\mathbf{T}_{\text{example}} = \begin{bmatrix} t_{12} & 0 \\ t_{23} & 0 \\ 0 & t_{45} \end{bmatrix}. \quad (2)$$

Short period interferograms constructed from acquisitions in 2004 are included in both time steps with the result that the rate estimates are not independent.

The inversion is weighted using a variance-covariance matrix $\Sigma_T$, to take into account atmospheric noise at each interferogram and correlation between interferograms. The element $\sigma_{lm-nq}$ of the variance–covariance matrix, $\Sigma_T$ represents the covariance between interferograms *lm* and *nq* and depends on the atmospheric error estimate for each interferogram $\sigma_{lm}$ and $\sigma_{nq}$ and the correlation between interferograms, $c_{lm-nq}$

$$\sigma_{lm-nq} = (\sigma_{lm}\sigma_{nq})c_{lm-nq}. \quad (3)$$

If the interferograms, *lm* and *nq*, have a common master or a common slave ($l = n$ or $m = q$), $c_{lm-nq} = 0.5$; if the master of one interferogram is the slave of the other ($l = q$ or $m = n$), $c_{lm-nq} = -0.5$ and at $l = n$ and $m = q$, $c_{lm-nq} = 1$. If the interferograms are independent, $c_{lm-nq} = 0$. For the sake of simplicity, the atmospheric error, $\sigma_{lm}$, on each interferogram is assumed to be constant, and the value chosen is 2.7 cm (from the 1-D covariance function analysis described later). Since the inversion is carried out on a pixel-by-pixel basis, it is not necessary to include the spatial correlation between pixels.

The inversion outputs rate maps and a map of the formal error for each time step (Fig. 3), and the covariance between the two time steps. In previous studies, such as Biggs *et al.* (2007), errors on each pixel of the rate map were assigned using formal errors from the inversion. The covariance between pixels was assumed to have the same decay parameters with distance as the individual interferograms. These assumptions are tested using a Monte Carlo method by constructing 100 sets of synthetic interferograms, composed only of atmospheric noise with no tectonic contribution.

The characteristics of the atmospheric noise on individual interferograms are estimated by calculating the 1-D covariance function and parametrizing it using the form:

$$c_{kl} = \sigma^2_{\max}(\mathrm{e})^{\frac{-r}{\alpha}} \mathrm{J}_0\left(\frac{2\pi \mathrm{r}}{\beta}\right), \quad (4)$$

where $c_{kl}$ is the covariance between pixels *k* and *l* a distance *r* apart, $\sigma_{\max}$ is the variance and $J_0$ is a zeroth-order Bessel function and $\alpha$ and $\beta$ are parameters which describe the spatial decay distance. This function allows for the 'hole' effect—a negative covariance at some distance before the covariance falls to zero at large distances (Armstrong 1998). The median parameters $\alpha = 25.8$ and $\beta = 152$ are similar to those found for the area in an earlier study using InSAR data from the ERS satellite (Biggs *et al.* 2007).

Synthetic atmospheric noise for each date in the time-series is generated based on the assumption that all dates are equally noisy such that the magnitude of the noise on any date is $1/\sqrt{2}$ of that on

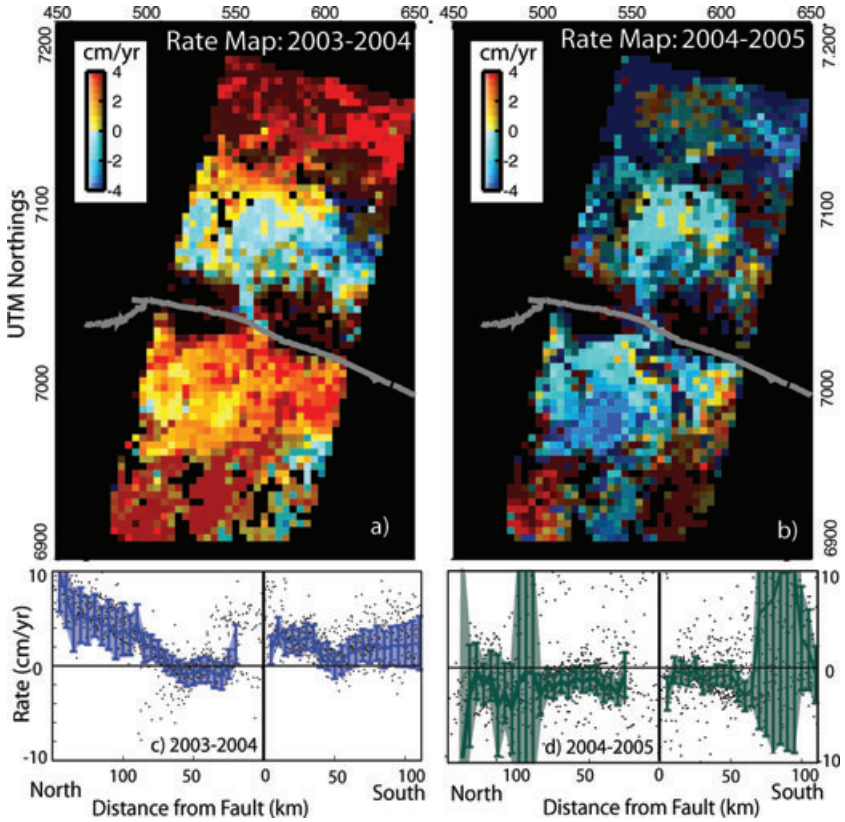


**Figure 3.** Rate maps for (a) 2003–2004 and (b) 2004–2005. The colours represent the rate at each pixel, and the intensity is inversely proportional to the estimated error (such that bright pixels have small errors and dull pixels have large errors). Profiles through the postseismic rate maps for (c) 2003–2004 (d) 2004–2005. Swath profiles are constructed using a weighted linear inversion on 5 km bins to estimate the best-fitting rate and associated error bar. Shaded region shows one sigma errors. Dots represent measurements from individual pixels. Long-wavelength errors may still be present as discussed in Section 3.3.

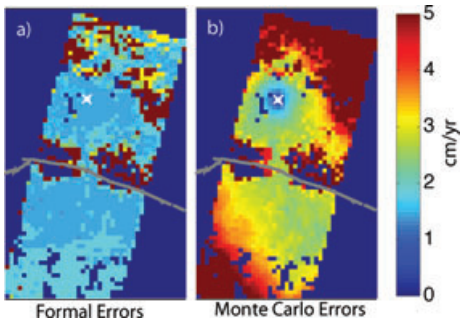


**Figure 4.** Comparison between (a) formal estimates and (b) Monte Carlo estimates for the error on each pixel of the 2003–2004 rate map. The white cross marks the location of the reference pixel.

an interferogram. A set of synthetic interferograms is created using masks based on the coherence of the original interferograms. The analysis algorithm is then applied to each of the data sets to create 100 rate maps. Since no tectonic signal is included in the synthetic interferograms, any non-zero values are the result of atmospheric noise.

A comparison between the Monte Carlo error (the standard deviation of the values at each pixel) and the formal error is shown in Fig. 4. Both error maps show the combined effects of error increasing with distance from the reference pixel (white crosses) and smaller errors for pixels which are coherent in more interferograms. However, the reference pixel effect is dominant in the Monte Carlo errors, and the coherence effect is dominant in the formal error. In general, the Monte Carlo errors are larger than the formal errors, especially in the far field, suggesting that the formal errors are underestimating the effects of the long-wavelength orbital errors. The errors of $\geq$4 cm yr$^{-1}$ in the far north and far south are much larger than the observed rates, indicating that the long-wavelength component of the displacement signal cannot be accurately determined due to this trade-off.

A 1-D covariance function is constructed for each of the rate maps and parametrized as before. The parameters $\alpha = 15.18$ km and $\beta = 181.53$ km are comparable to those of an individual interferogram. Combining the interferograms does not significantly affect the structure of the atmospheric noise, but does reduce the magnitude.

### 3.3 Observed displacement

The rate map for 2003–2004 (Fig. 3a) shows a similar spatial pattern to the simple stacked approach with positive line-of-sight range changes to the south of the fault and negative to the north. As before, peak displacements occur at a distance of ∼50 km from the fault with peak-to-trough displacements of ∼4 cm yr$^{-1}$. The rate map for 2004–2005 shows no clear spatial pattern, suggesting that the rapidly decaying postseismic transient has fallen below the threshold observable using InSAR by this time.

Profiles through the rate map (Figs 3c and d) are constructed using a weighted least-squares inversion to find the best-fitting rate and associated error in 5 km bins, distributed according to distance from the nine segment fault geometry defined in Table 1. The variance–covariance matrix between pixels is constructed using the errors and covariances from the Monte Carlo analysis such that $\sigma_{kl} = c_{kl}\,\sigma_k\,\sigma_l$, where $\sigma_k$ and $\sigma_l$ are the error estimates for individual pixels and $c_{kl}$ is the correlation coefficient between them, calculated using eq. (3).

The asymmetry seen in the stacked profiles is preserved, with the peak displacement occurring significantly closer to the fault to the south than to the north. Unlike the stacked result (Fig. 2) in which the far-field displacements were artificially fixed to be small, there is still a long-wavelength component to these profiles due to the residual orbital contribution from the network orbital correction. Since the data coverage does not extend sufficiently far from the fault to define areas of zero displacement, the long-wavelength contribution is removed at a later stage by minimizing the linear long-wavelength misfit to the model. Far-field GPS data have been shown to have important discriminating capabilities in previous studies of postseismic deformation (Freed *et al.* 2007), but due to the trade-offs with orbital errors when observing long-wavelength displacements using InSAR, we do not consider the far-field displacements in this study to be sufficiently well determined to place constraints on our models.

Sections 4–7 of this paper compare the 2003–2004 rate map shown in Fig. 3(a) to rates from a range of possible models.

### 3.4 Vertical component

Previous studies have shown that measurements of the vertical component of deformation can be key to distinguishing between the postseismic response due to afterslip and viscoelastic relaxation

**Table 1.** Table showing coseismic input parameters for the 2002 Denali Fault earthquake (D1–D7) from Wright *et al.* (2004), Susitna Glacier Fault (SGF) subevent, Nenana Mountain earthquake (NME) and Delta River earthquake (DREa–c). Distances (length, top and bottom depths) are given in kilometres and slip in metres.

| Event | Strike | Dip | Rake | Slip | Length | Top | Bottom | Long | Lat |
|---|---|---|---|---|---|---|---|---|---|
| D1 | 98.3 | 90 | 180 | 2.4 | 47.0 | 0 | 14.3 | 146.282 | 63.476 |
| D2 | 105.1 | 90 | 180 | 5.7 | 20.3 | 0 | 14.3 | 145.890 | 64.427 |
| D3 | 119.0 | 90 | 180 | 5.0 | 22.2 | 0 | 14.3 | 145.505 | 63.326 |
| D4 | 108.4 | 90 | 180 | 8.7 | 31.6 | 0 | 14.3 | 144.912 | 63.232 |
| D5 | 114.9 | 90 | 180 | 5.8 | 39.6 | 0 | 14.3 | 144.207 | 63.073 |
| D6 | 116.8 | 90 | 180 | 7.5 | 51.5 | 0 | 14.3 | 143.319 | 62.849 |
| D7 | 151.2 | 90 | 180 | 2.9 | 20.8 | 0 | 14.3 | 143.149 | 62.672 |
| SGF | 249.6 | 41.0 | 84.6 | 7.3 | 28.5 | 1.3 | 9.5 | 147.699 | 63.487 |
| NME | 262 | 81 | 174 | 1 | 21.5 | 5.2 | 20.6 | 148.260 | 63.463 |
| DREa | 98.3 | 90 | 180 | 2.1 | 47.0 | 0 | 14.3 | 146.282 | 63.476 |
| DREb | 105.1 | 90 | 180 | 2.1 | 20.3 | 0 | 14.3 | 145.890 | 64.427 |
| DREc | 119.0 | 90 | 180 | 2.1 | 22.2 | 0 | 14.3 | 145.505 | 63.326 |

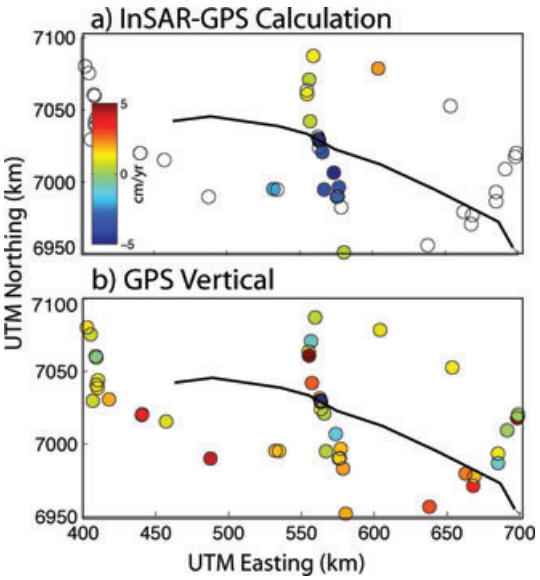


**Figure 5.** Estimates of vertical motion for 2003–2004. (a) Calculation from InSAR data and the horizontal components of GPS-measured displacements at sites within the SAR frame. Empty circles are GPS sites outside the InSAR swath. (b) GPS estimates of vertical motion.

(Pollitz *et al.* 2001; Freed *et al.* 2006a). Using the horizontal GPS measurements, together with the InSAR line-of-sight displacements, it is possible to calculate the vertical displacement at all collocated sites (Fig. 5). The InSAR–GPS estimates of vertical motion can be compared to the GPS-measured vertical rates (Fig. S3).

The errors on the InSAR–GPS calculated vertical rate are dominated by uncertainties in the InSAR and are, in some cases, several times larger than the formal errors on the vertical GPS components. The InSAR–GPS calculated rates are systematically lower because the measurements are relative to a reference pixel to the north of the fault. Taking this offset and the size of the formal errors into account, the estimates are within the range of GPS observations of vertical motion. However, although the InSAR–GPS vertical components show a geographical pattern with subsidence to the south of the fault and uplift to the north (Fig. 5a), there is no similar pattern in the GPS vertical measurements (Fig. 5b) because of distorted satellite orbits resulting from inaccuracies in the GPS satellite antenna phase centre models. Mismodelling of satellite antenna phase centres, especially for a new model of GPS satellite that came increasingly into use beginning in 2003, causes an apparent increase in uplift rate during 2003–2006 at all sites in the near polar regions, including sites in Alaska (but not sites in mid-latitudes). Relative GPS vertical velocities show better agreement with the InSAR data and with postseismic model predictions, although the InSAR–GPS comparison remains dominated by uncertainties in the InSAR rate (Fig. S3).

## 4 RELAXATION OF A VISCOELASTIC MEDIUM

To evaluate the contributions from lower-crustal and mantle relaxation, we consider first-order, elastic layer over viscoelastic (Maxwell) layered rheologies.

For relatively short time periods, a Maxwell (linear) rheology can be used to model the spatial pattern of postseismic displacements and estimate an effective viscosity. If the rheology is non-linear or transient, the effective viscosity may be stress- and time-dependent (Freed *et al.* 2006b). For the DF study, the data used cover the time period between 18 and 30 months after the earthquake. Analysis of the postseismic response to the 1997 Manyi, Tibet earthquake (Ryder *et al.* 2007) shows that the effective Maxwell viscosity may change by roughly a factor of three, during the first 3–4 yr after an earthquake. The additional errors associated with modelling a more complex rheology with a single, time-invariant Maxwell rheology over such a short time period, are less significant than the inherent uncertainties in the geometry of the model and the resulting trade-offs. Previous models of viscoelastic relaxation following the DF earthquake have been based on horizontal estimates of displacement from GPS. The use of InSAR rate maps allows us to include constraints on the vertical component of motion for the first time.

### 4.1 Model setup

We use VISCO1D (Pollitz 1992) to calculate the surface displacements resulting from the stresses imposed by the DF earthquake on a range of layered viscoelastic rheologies. The fortran code computes internal or surface displacements at user-specified times following the earthquake, for a user-specified earth model and set of fault parameters. In all models, the elastic shear modulus is held constant at 40 GPa and the density structure modified from the Preliminary Reference Earth Model (PREM) (Dziewonski & Anderson 1981). The coseismic input parameters are based on the slip model of Wright *et al.* (2004) from a joint inversion of GPS and InSAR which divides the DF into nine segments along strike, each of which has a uniform amount of slip. Of these, we use seven segments corresponding to the sections of the Denali and Totschunda Faults, which ruptured during the 2002 earthquake (Table 1). The thrust motion on the SGF is treated as a separate subevent. The contribution of this and the Nenena Mountain foreshock are considered later.

### 4.2 Two-layer models

Initially, we consider a simple two-layer rheological structure composed of an elastic lid of thickness $H$ over a viscoelastic half-space of viscosity $\eta$. Forward models are calculated for a range of viscosities, $5 \times 10^{17} < \eta < 7 \times 10^{19}$ Pa s, and elastic lid thickness, $10 < H < 70$ km. For each rheological structure, the residual between model and InSAR rate map is calculated, and the best-fitting quadratic function estimated. This is removed from the observations to adjust for any remnant orbital error. Each forward model is then compared to correspondingly adjusted InSAR observations, to find the weighted root mean square misfit. The weighted misfits are contoured and plotted in Fig. 6. Misfits to the horizontal GPS data were calculated independently and show similar patterns.

The dominant feature of the weighted rms misfit plots is the trade-off between lid thickness and viscosity. For 2003–2004, surface displacements can be matched with either a thin lid (10 km) overlying a high viscosity ($1 \times 10^{19}$ Pa s) half-space or a thick lid (70 km) overlying a low-viscosity half-space ($5 \times 10^{17}$ Pa s). Due to this trade-off, the weighted misfit is not sensitive to the thickness of the elastic lid; the slight decrease in misfit for elastic lids of 40–60 km is not considered significant.

For the period 2004–2005, the profile across the rate map (Fig. 3d) showed that the displacement rates were not significantly larger than the measurement errors. Consequently, there is no minimum in the weighted rms misfit plot, with the smallest misfits being for models

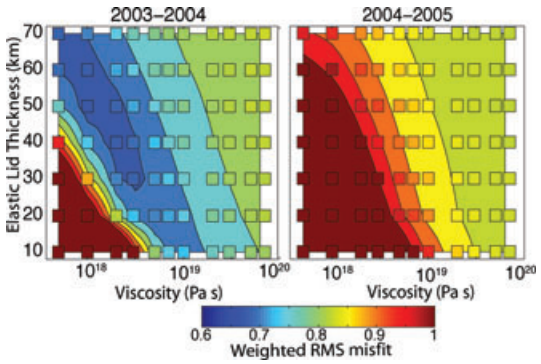


**Figure 6.** Weighted rms misfits for a range of viscoelastic forward models composed of an elastic lid of thickness $H$, overlying a viscoelastic half-space of viscosity $\eta$. A quadratic function is estimated from the residual and removed from the rate map to adjust for any remnant orbital error. Squares represent the results of model runs, which are then interpolated onto a finer grid.

with large elastic lids and high viscosities and, correspondingly, the smallest displacements. This suggests that the postseismic response has decayed to the point where the displacements cannot be resolved using the available InSAR data spanning a single year.

The thickness of the elastic lid has a significant effect on the dominant wavelength of the deformation field, and profiles perpendicular to the fault can be used to distinguish between models (Fig. 7). For each lid thickness (10–70 km), the best-fitting viscosity is chosen from the weighted misfit plot and swath profiles through the corresponding models, and the adjusted rate maps are calculated. As before, a weighted linear inversion is used to estimate the mean value for each bin. The inversion is weighted using the estimated Monte Carlo error on each pixel and covariances based on a parametrized 1-D covariance function.

The wavelength of the observed displacements is best approximated by an elastic lid thickness of ∼50 km, with a lower-layer viscosity of $1 \times 10^{18}$ Pa s. This result, derived from InSAR data alone, is consistent with the results of previous GPS-only studies, such as Freed *et al.* (2006a). Given that the Moho depth in this region is estimated to be 40–50 km (Brocher *et al.* 2004), this is consistent with relaxation in the upper mantle. This does not imply that the lower crust is elastic, only that the dominant response on this timescale occurs in the upper mantle. The rheology of the lower crust is investigated in more detail in Section 4.4. Each model systematically underestimates the magnitude of the displacements to the north of the fault and overestimates those to the south.

### 4.3 Viscoelastic contribution from subevents and previous earthquakes

Previous earthquakes in the region may also contribute to the displacement field. Significant events in the region are the $M_w$6.7 Nenana Mountain foreshock, the $M_w$7.2 SGF subevent and the $M$ 7.2–7.4 Delta River earthquake in 1912. Between 1912 and 2002, the level of recorded seismicity on this section of the DF was

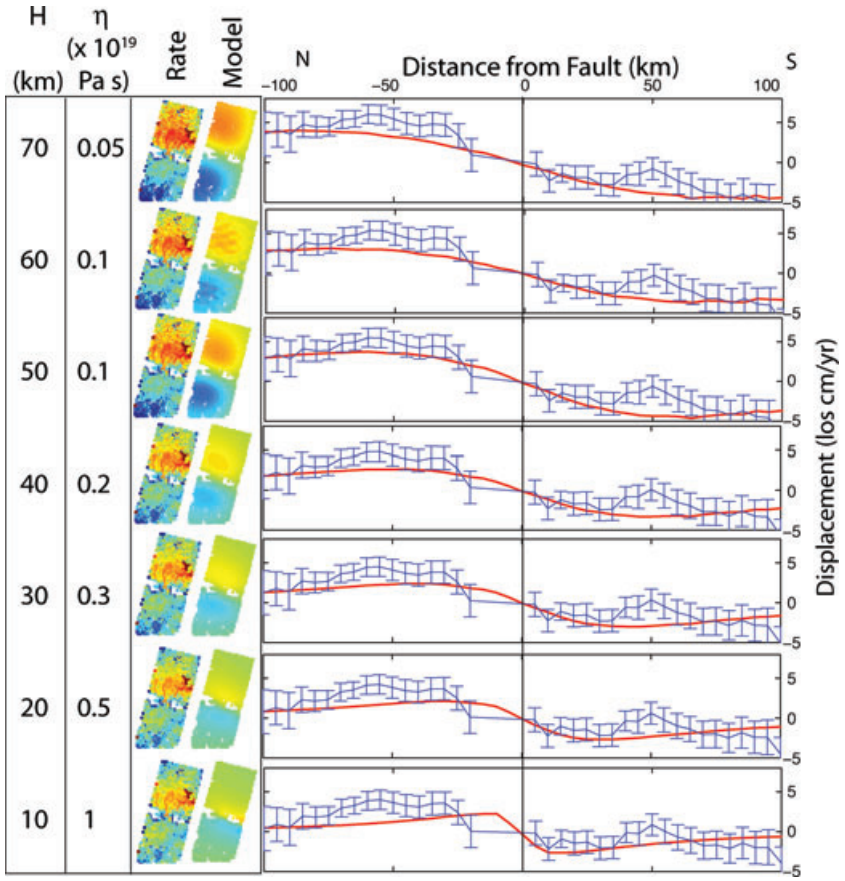


**Figure 7.** Fault-normal profiles through two-layer viscoelastic models (red line) and comparison to binned swath profiles through the 2003–2004 rate map with errors (blue bars) For each elastic lid thickness, the weighted rms misfit (Fig. 6) is used to choose the best-fitting viscosity. The InSAR line-of-sight measurements are dominated by the vertical component of displacement.

very low. The best-fitting two-layer rheology already determined—a 50 km thick elastic lid over a viscoelastic half-space with a viscosity of $1 \times 10^{18}$ Pa s—is used to make predictions for the displacement resulting from each event for the period between summer 2003 and summer 2004.

Coseismic parameters for the Nenana Mountain earthquake and SGF subevents are taken from the geodetic inversions of Wright *et al.* (2003) and Wright *et al.* (2004), respectively, and given in Table 1. From a combination of tree damage, felt intensity and seismology, Carver *et al.* (2004) conclude that the epicentre of the Delta River earthquake was located close to the present location of the Richardson highway, and the rupture propagated unilaterally westwards for a distance of 60–84 km, with an average horizontal slip of 1.4–2.1 m. To replicate the largest possible event consistent with the data, the earthquake is assumed to have ruptured the three western segments of the DF, with an average slip of 2.1 m.

The predicted displacements contributed by the SGF subevent are an order of magnitude smaller than those from the DF earthquake (Fig. 8b), while those resulting from the Nenana Mountain Foreshock (Fig. 8c) and Delta River earthquake are two orders of magnitude smaller (Fig. 8d). Although more comparable in magnitude to the 2002 DF earthquake, the Delta River earthquake occurred 90 yr ago. On the timescale of the observations used here, less than 4 yr after the 2002 earthquake, the surface deformation field is dominated by the DF main event.

### 4.4 Three-layer models

The optimum two-layer model is consistent with viscoelastic relaxation that occurs dominantly in the upper mantle (below 50 km). However, previous studies of other earthquakes (Hearn *et al.* 2002; Ryder *et al.* 2007) have found that viscoelastic relaxation occurred in the lower crust. Here, we consider a lower crust which is viscoelastic but with a higher viscosity than the lower mantle. To account for a high viscosity lower crust, some previous authors (e.g. Pollitz 2005) have fixed a constant ratio of viscosity between the upper mantle and lower crust. We fix the dimensions of a three-layered rheology from additional information and explore a range of viscosities. For these models, the upper layer is an elastic lid of thickness 15 km, consistent with the thickness of the seismogenic zone from coseismic (e.g. Wright *et al.* 2004; Hreinsdottir *et al.* 2006) and aftershock studies (Ratchkovski *et al.* 2004). The second layer is viscoelastic and corresponds to the lower crust with viscosities ranging between $\eta_{\rm lc} = 1 \times 10^{18}$ Pa s (the best-fitting upper mantle viscosity) and $\eta_{\rm lc} = 1 \times 10^{29}$ Pa s (essentially elastic). The final layer is a viscoelastic half-space corresponding to the upper mantle and whose upper boundary is at 50 km, consistent with estimates of Moho depth (Brocher *et al.* 2004). A range of viscosities are tested for the upper mantle, to allow for trade-offs between the two layers, but the best-fitting viscosity of $\eta_{\rm um} = 1 \times 10^{18}$ Pa s, estimated from the two-layer models, still provides the best fit.

As for the two-layer models, the best-fitting quadratic polynomial is estimated from the misfits and removed from the rate map. Profiles across the models and observations are constructed as before and shown in Fig. 9. For a model with lower-crustal viscosity of $\eta_{\rm lc} = 10^{18}$ Pa s, the lower crust and upper mantle have the same viscosity, and the model behaves the same as a two-layer model with an

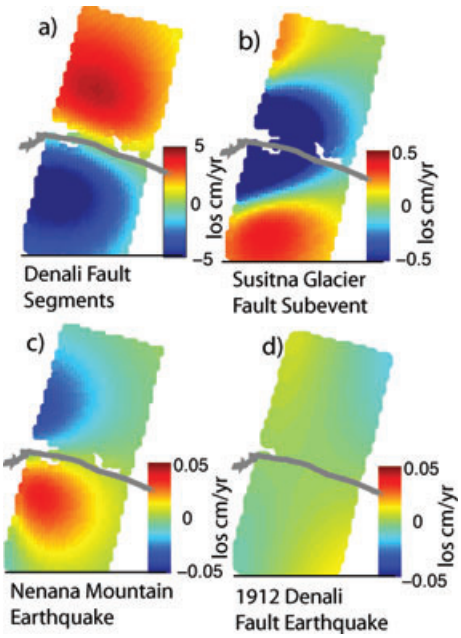


**Figure 8.** Predictions for the line-of-sight displacement rate for 2003–2004 due to the postseismic response to the Nenana Mountain foreshock, Susitna Glacier Fault subevent and 1912 Delta River earthquake. Models use a two-layer rheology with a 50 km elastic lid over a viscoelastic half-space with a viscosity of $1 \times 10^{18}$ Pa s.

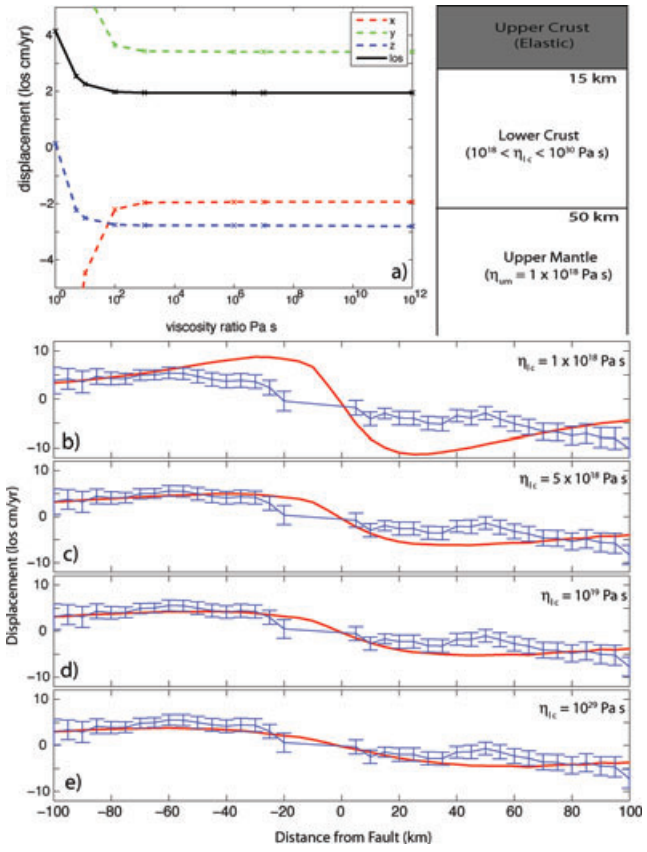


**Figure 9.** (a) Displacements for a given pixel for a range of viscosity ratios, $\frac{\eta_{\rm lc}}{\eta_{\rm um}}$. For ratios in excess of ∼1000, the lower crust behaves essentially elastically. (b–e) Profiles through rate map and three-layer models for 2003–2004. The viscosity of the lower crust (15–50 km) is different in each model. (b) $\eta_{\rm lc} = 10^{18}$ Pa s—uniform viscosity in lower crust and upper mantle. (c and d) Lower-crustal viscosity is larger than upper mantle viscosity. (e) $\eta_{\rm lc} = 10^{29}$ Pa s—lower-crustal viscosity so high it is essentially elastic.

elastic lid thickness of 15 km and a half-space viscosity of $1 \times 10^{18}$ Pa s. The model deformation has a much larger amplitude and smaller wavelength than the observations. At the other extreme, the model with a viscosity of $\eta_{\rm lc} = 10^{29}$ Pa s has an essentially elastic lower crust and is equivalent to the best-fitting two-layer model, with an elastic lid 50 km thick. The other models have a lower-crustal viscosity intermediate between elastic and the upper-mantle viscosity. The amplitude of the signal decreases with increasing viscosity until a viscosity ratio of $\frac{\eta_{\rm lc}}{\eta_{\rm um}} \sim 10^3$ is reached (Fig. 9). Numerically, the minimum weighted rms is for an elastic lower crust, but a qualitative assessment of the profiles shows no improvement in fit for viscosity ratios $\frac{\eta_{\rm lc}}{\eta_{\rm um}} \geq 5$.

## 5 AFTERSLIP ON A DISCRETE PLANE

Instead of or in addition to viscoelastic flow, localized shear or afterslip may contribute to postseismic deformation. We perform an inversion of the geodetic data for afterslip on a discrete plane. The interferograms considered here are from a single track and, therefore, only cover a limited section of the rupture. To provide more comprehensive coverage and stabilize the afterslip inversion, we perform a joint inversion of the InSAR rate map and horizontal displacement vectors from continuous and campaign GPS data. The use of the InSAR rate map means that the afterslip model is sensitive to vertical displacements in the region of the pipeline. GPS sites south of 62°N are likely to be affected by deformation associated with the subduction zone and are not included.

### 5.1 GPS–InSAR inversion method

A kinematic afterslip inversion is carried out using a linear inversion for slip distribution using a modified version of the 'slipinv' code (Funning *et al.* 2005). For the eight segments representing the Denali and Totschunda Faults, the coseismic geometry is retained for the afterslip inversion but with the depth extended down to 60 km. The geometric configuration between the SGF and DF at depth is poorly known, but the downward continuation of the northward dipping SGF would intersect the vertical DF. Consequently, we assume that the SGF is a splay from the main DF and solve for afterslip on a vertical fault under the surface trace of the DF.

A linear inversion of the form $\mathbf{Gm} = \mathbf{d}$ is used to solve for the slip on each patch, $m$, using both measurements of surface displacement from both InSAR, $d_{\rm INS}$ and GPS, $d_{\rm GPS}$ such that $\mathbf{d} = [d_{\rm INS}, d_{\rm GPS}]^T$. The design matrix, $\mathbf{G}$, for the inversion is composed of the Green's functions for GPS and InSAR, smoothing constraints and orbital adjustments.

$$\mathbf{G} = \begin{pmatrix} G_{\rm INS} & x_i & y_i & x_i^2 & y_i^2 & x_i y_i & 1 \\ G_{\rm GPS} & 0 & 0 & 0 & 0 & 0 & 0 \\ \nabla^2 & 0 & 0 & 0 & 0 & 0 & 0 \end{pmatrix}. \quad (5)$$

$G_{\rm GPS}$ and $G_{\rm INS}$ are the Green's functions for the GPS and InSAR, respectively, which relate unit slip on each fault patch within the model geometry to each surface observation. Since there is likely to be a residual orbital error in the data, we include nuisance parameters allowing for an additional quadratic polynomial and offset, $z = ax + by + cx^2 + dy^2 + exy + f$ on the InSAR data, where $x$ and $y$ are the Cartesian distances from a reference pixel. A second-order Laplacian smoothing constraint, $\nabla^2$ is added to prevent rough slip distributions.

While the DF is dominantly strike-slip, modelling of the coseismic displacements shows a variable component of dip-slip movement along the fault (Hreinsdottir *et al.* 2006; Elliott *et al.* 2007). To allow for similar variation in rake in the afterslip solution, we solve for two components with rakes of 135° and −135°, respectively, using a non-negative least-squares algorithm, allowing for slip directions up to 45° either side of pure strike-slip. The vector sum of the components gives the total displacement at each patch.

Error estimates associated with each observation are used to construct a variance–covariance matrix to weight the inversion. For the InSAR, the elements of the variance–covariance matrix are calculated using the Monte Carlo estimate of the error on each pixel and a parametrized 1-D covariance function. Off-diagonal components resulting from correlations between north and east GPS components and between pixels in the InSAR are included, but there is no correlation between InSAR and GPS measurements. Assuming that the errors on each observation are correctly assigned to weight the inversion, further weighting between the GPS and InSAR data sets is not necessary. The relative weighting of the smoothing function is estimated using a trade-off curve between roughness and misfit (Fig. 10a), where the roughness is estimated using the Laplacian of the solution.

### 5.2 Model depth

Long-wavelength components in the InSAR data can be explained equally well by very deep slip, or orbital errors, that is, there are significant trade-offs between model parameters and observational errors. The depth to which slip would occur is not clear from physical considerations, especially since at depths corresponding to the mantle, slip on the fault plane is often regarded as a proxy for a more distributed deformation mechanism. Using synthetic examples, Ryder *et al.* (2007) show that when the allowed depth is shallower than the imposed slip, the misfit is high, but as the inversion depth

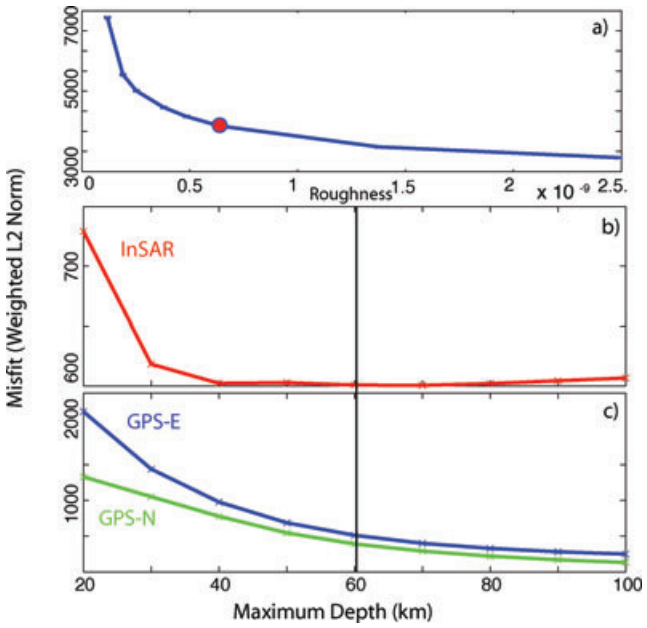


**Figure 10.** Model misfit for a range of different smoothing parameters and inversion depths. (a) Trade-off curve between weighted norm and roughness of slip distribution. The red dot marks the chosen smoothing parameter. (b) Misfit to InSAR data showing high values for maximum depths of less than 40 km and a slight minimum at 60–70 km. (c) Misfit to GPS data showing a gradual decrease in misfit with increasing depth. A maximum depth of 60 km is chosen for the inversion.

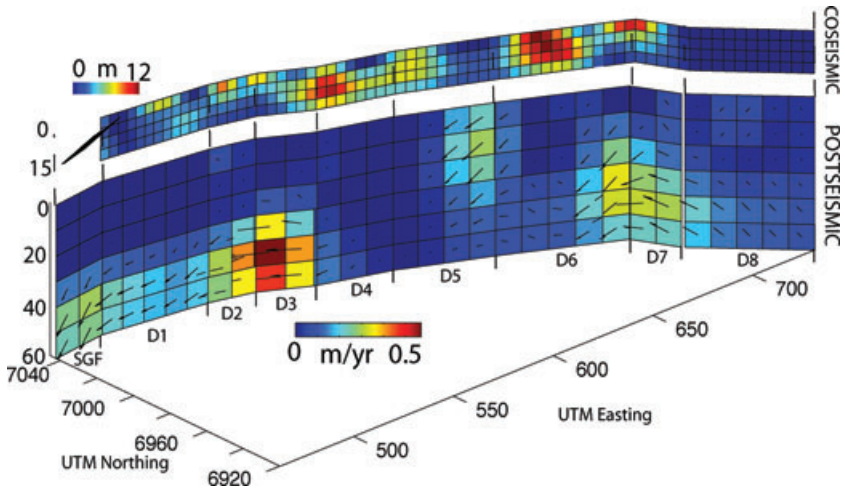


**Figure 11.** Preferred afterslip model for the period summer 2003–summer 2004 based on a joint inversion of InSAR and GPS data. The coseismic model is from the InSAR–GPS inversion of Wright *et al.* (2004). Note the coseismic model extends to a depth of 15 km while the postseismic model extends to 60 km.

increases, the fit improves. When the allowed depth is greater than the imposed depth, the misfit remains low. In the case of Denali, the GPS misfit continues to decrease as the maximum depth increases (Fig. 10c). The InSAR misfit is large for depth limits less than 40 km, and generally low beyond that with a slight minimum at 60–70 km (Fig. 10b). The difference in behaviour is not related to the relationship between slip at depth and surface displacements, since this is independent of the observation technique, but results from the orbital adjustments made for the InSAR data, which trade-off against deep slip. A maximum depth of 60 km is chosen.

### 5.3 Afterslip inversion results

Fig. 11 shows the afterslip model for the period from summer 2003 to summer 2004 from a joint inversion of InSAR and GPS data. The coseismic slip model of Wright *et al.* (2004) is shown for comparison. Most of the afterslip occurs at depths below 40 km which corresponds with the uppermost mantle in this region (Brocher *et al.* 2004). The peak slip is ∼80 cm but typical values are ∼30 cm. The sense of motion is almost pure right-lateral strike-slip. Comparison between the coseismic and postseismic inversions shows that the patch of shallow afterslip at the eastern end of segment D5 corresponds to an area of coseismic low slip, surrounded by high slips. This is consistent with a stress-driven afterslip model in which stress is built-up on the locked patch during the earthquake and released aseismically afterwards. The area of highest postseismic slip occurs in segment D3, immediately to the west of the coseismic high slip patch in segment D4 [subevent 2 in the classification of Eberhart-Phillips *et al.* (2003)]. There is an area of high slip in both the coseismic and postseismic models at D6–D7 which corresponds to the step over between the Denali and Totschunda Faults, but it is difficult to distinguish between the physical signal associated with the complex fault interactions and model artefacts resulting from an oversimplification of the fault geometry. The model data and misfits are shown in Fig. 12.

### 5.4 Model errors

The variability in the solution caused by atmospheric noise in the InSAR data can be estimated using a Monte Carlo method. One hundred sets of synthetic atmospheric noise are constructed for each

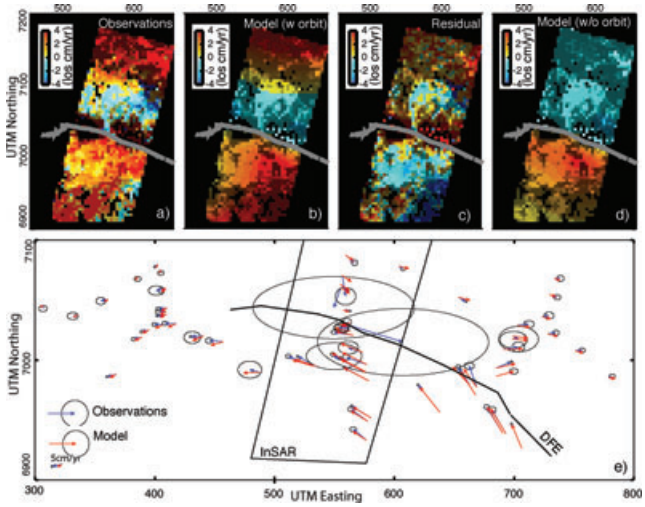


**Figure 12.** Misfit of afterslip model to observed data (a) InSAR observations plotted as a rate map. The pixel intensity is proportional to the inverse of the variance such that bright pixels have small errors and dull pixels have large errors. (b) Afterslip model predictions including orbital contributions, (c) residual, (d) afterslip model predictions without orbital contributions and (e) GPS model and observations.

date in the time-series using the parametrized 1-D covariance function, estimated from the individual interferograms and the method of Parsons *et al.* (2006). These are combined with the original interferograms to produce 100 sets of perturbed interferograms. Each set of perturbed interferograms is used to produce a rate map for which a model of fault slip is estimated. The standard deviations of the values for each component (component 1: rake = 135°, component 2: rake = −135°) and each patch of the resulting slip model are shown in Fig. 13. The Monte Carlo errors on the slip are an order of magnitude smaller than the slip values, indicating that the atmospheric noise on the interferograms has a small effect and that the GPS alone controls the major features of the slip distribution. The Monte Carlo errors are highest where the slip is highest, since where the slip is small, or zero, the range of acceptable slip values is smaller.

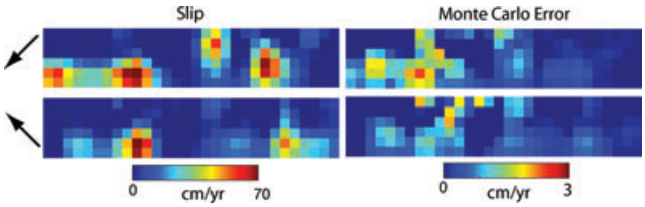


**Figure 13.** Monte Carlo error estimates on each patch of the fault. Two components with orthogonal rakes (denoted by arrows on the left) are shown. The Monte Carlo errors are an order of magnitude smaller than the estimated slip, showing that atmospheric errors on the InSAR data have little impact on the solution in comparison with the controlling influence of the GPS.

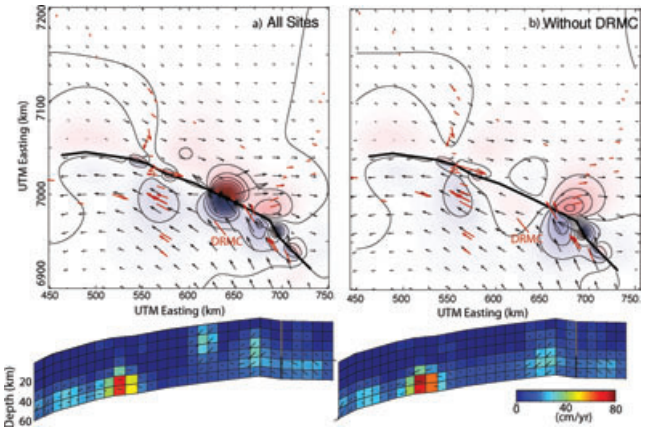


**Figure 14.** Dependence of shallow afterslip signal on individual sites. Colours represent the modelled vertical motions, with contours every 1 cm yr$^{-1}$. Black arrows represent modelled horizontal displacements, and red arrows represent measured displacements at GPS sites. The earthquake rupture is shown in black. (a) Inversion result using all GPS sites with shallow afterslip of ∼40 cm yr$^{-1}$ causing vertical displacements of ±15 cm yr$^{-1}$ at the surface. (b) Inversion result without site DRMC.

### 5.5 Origin of shallow signal

The models include a patch of shallow afterslip at depths of 10–30 km in segment D5, which would produce vertical motions of ±15 cm yr$^{-1}$ at the surface. This signal occurs in a region with few GPS stations and no InSAR, and it is important to test the robustness of the result by removing individual GPS sites from the inversion. By removing site DRMC, the shallow afterslip signal on segment D5 disappears (Fig. 14), but a large residual to the observed DRMC motion of 9 mm east and 31 mm north is created (compared to 2 mm east and 3 mm north when DRMC is included in the inversion). DRMC is a cGPS site, so has small errors, and no instrumental reason is known for any unusual motion. Previous models of poroelastic rebound for this earthquake (Freed *et al.* 2006b) predict very small displacements except very close to the fault and around the junction between the Denali and Totschunda Faults. Since the signal is observed at just one GPS location, it is difficult to distinguish between possible causative mechanisms, and it is impossible to rule out a shallow poroelastic response or station artefact.

## 6 MIXED MECHANISM MODEL

Until this point, we have explored two independent mechanisms of postseismic deformation: afterslip and viscoelastic relaxation. Now we consider the possibility that both mechanisms occur but in spatially distinct layers: afterslip in the crust and viscoelastic relaxation in the mantle (e.g. Johnson *et al.* 2008).

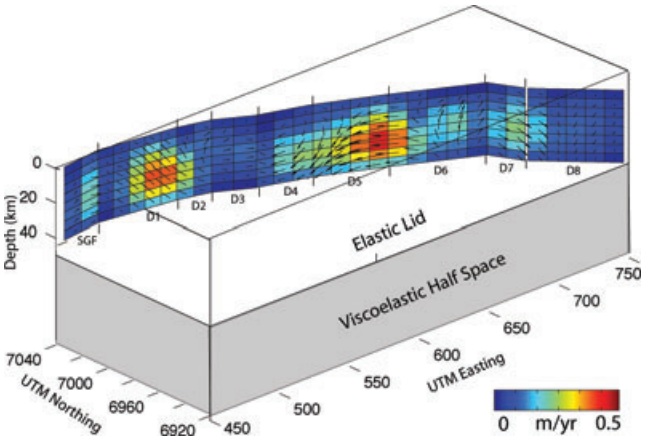


**Figure 15.** Mixed mechanism model for postseismic displacements with afterslip in the crust and viscoelastic relaxation in the mantle. The viscoelastic model has an elastic layer thickness of 50 km over a half-space with viscosity $10^{18}$ Pa s.

To model this, we start by estimating the displacements caused by viscoelastic relaxation beneath an elastic lid using VISCO1D (Pollitz 1992). These estimates are removed from both the InSAR and GPS data, and a linear inversion is applied to find any additional afterslip in the crust. In all cases, we restrict afterslip to the upper 40 km, equivalent to the crust, but we vary the thickness of the elastic lid used in the viscoelastic calculation, to investigate the trade-off between the two mechanisms. Unlike the previous afterslip inversion, we do not use a non-negativity constraint and allow slip in any direction.

The lowest misfits are found for low-viscosity, thick-lid models, since in these cases, any surface displacements not explained by the viscoelastic model can be attributed to shallow afterslip. Fig. 15 shows the afterslip distribution for the optimum viscoelastic model determined in the previous section (an elastic thickness of 50 km and a viscosity of $10^{18}$ Pa s). In general, the afterslip is less than 20 cm yr$^{-1}$, with two exceptions. The 40–50 cm yr$^{-1}$ of slip in segment D5, corresponds to the shallow signal discussed in Section 5.5. Slip of approximately 30 cm yr$^{-1}$ occurs in segment D1, close to the location of peak slip in the pure afterslip model.

## 7 ORIGIN OF ASYMMETRY IN POSTSEISMIC DISPLACEMENT FIELD

A significant asymmetry is seen in the profiles of postseismic displacements observed by InSAR (Fig. 7). Each model systematically underestimates the magnitude of the displacements to the north of the fault and overestimates those to the south. This asymmetry is opposite in sense to that observed by GPS which shows larger, more slowly-decaying horizontal displacements to the south of the fault. Fault curvature, differences in rheological structure and the presence of an elastic slab in the mantle are all possible causes of asymmetry in the postseismic displacements. The models in the previous section take into account the curvature of the DF, and while some asymmetry is predicted, the models are not capable of matching the extent of asymmetry observed. The presence of a subducted slab within the mantle in the western region of the rupture may imply that models based on a simple layered rheology are not appropriate.

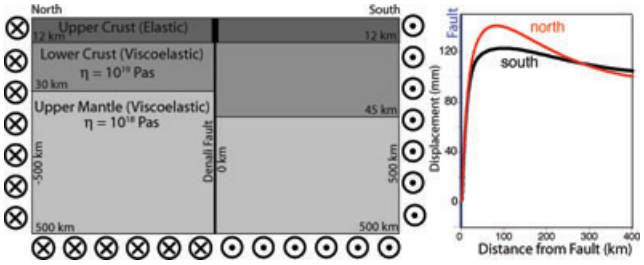


**Figure 16.** Finite-element model to investigate the asymmetry generated in the postseismic displacement field by differences in Moho depth. (a) Idealized rheological structure in cross-section normal to the fault. Displacements take place out of the plane of the cross-section. (b) Fault-parallel horizontal displacements predicted for the time period between 1.5 and 2.5 yr after the earthquake.

The DF is an inherited structure which originally formed as the boundary between accreted terranes with the Yukon-Tanana Composite Terrane to the north of the fault and the Wrangellia Terrane to the south (Plafker *et al.* 1994). We conclude that differences in rheological properties are likely to be the primary cause of asymmetry. The Trans-Alaska Crustal Transect (TACT) seismic lines suggest that the Moho depth in this region is transitional between thick crust under the Alaska Range (40–50 km) and thin (28–32 km), low-velocity (6.1–6.4 km $s^{-1}$) crust in the Yukon-Tanana Terrane (Brocher *et al.* 2004). Further west along the terrane boundary, receiver function analysis found typical crust to the north to be 26 km thick but a thickness of 35–45 km to the south. This difference can be explained using Airy isostasy for a crustal density change of 4.6 per cent across the boundary (Veenstra *et al.* 2006).

We use a finite-element model to investigate the effect of varying Moho depth on postseismic displacements (Fig. 16). We use the finite-element code G-TECTON (Melosh & Raefsky 1980; Govers 1993; Schmalzle *et al.* 2006). The model structure is a cross-section normal to the fault and allows for displacements, but not displacement gradients, in an out-of-plane direction—a '2.5D' model (Schmalzle *et al.* 2006). The rheological structure is idealized to the following layers: (1) an elastic upper crust of thickness 12 km; (2) a Maxwell viscoelastic lower crust with a viscosity of $10^{19}$ Pa s to a depth of 30 km to the north of the fault, and 45 km to the south and (3) a Maxwell viscoelastic layer representing the mantle with a viscosity of $10^{18}$ Pa s, extending from the base of the crust to a depth of 500 km, to simulate a half-space. We use a fixed Young's modulus of 100 GPa and a Poisson's Ratio of 0.25 for all layers. The fault extends through the elastic layer, and a displacement of 9 m is applied every 900 yr on the locked fault via the split node method (Melosh & Raefsky 1981). The earthquake repeat time is calculated assuming a characteristic earthquake cycle, with a fault slip rate of 10 mm $yr^{-1}$ (Biggs *et al.* 2007) and earthquake slip of 9 m. To reduce the impact of edge effects, the model is extended to a distance of 500 km on either side of the fault.

The lower, northern and southern boundaries are constrained to move only in a fault-parallel (out-of-plane) direction, and the upper surface is free. We use a higher density of nodes around the fault where high stresses are known to occur. Node spacing is tested to that ensure mesh effects are not significant. Time steps of 0.5 yr are used for the 2.5 yr following an earthquake and 5 yr for the rest of the earthquake cycle. We also compare results using time steps of 0.25 yr to check that no artefacts are introduced. We run the model for a total of 10 earthquake cycles to allow the system to reach equilibrium and check for convergence.

We differentiate the fault-parallel displacements at 1.5 and 2.5 yr after the earthquake to match the timing of our InSAR and GPS observations (Fig. 16). A comparison of the displacements on either side of the fault shows a sharper peak to the north of the fault and a broader plateau to the south. Also, the near-field displacements are larger to the north, and the far-field displacements are larger to the south. Qualitatively, these predictions are consistent with our observations that (1) the peak in line-of-sight InSAR displacements is sharper in the north and broader in the south and (2) models of horizontally stratified rheology with no lateral changes in material properties underestimate the displacements to the north, and overestimate those to the south. A quantitative comparison would require a full 3-D fault model to take into account the variation in slip along strike and the curvature of fault, which are responsible for the vertical component of displacement. The errors on the InSAR profile are significant and more complex models, while interesting theoretically, are not warranted for this data set.

## 8 DISCUSSION

### 8.1 Postseismic mechanism

A number of current scientific questions depend on the rheology of the lithosphere. Observation of postseismic relaxation is one of the few ways in which this can be studied *in situ* (Bürgmann & Dresen 2008). The model of viscoelastic relaxation uses the relationship between stress and strain in a viscoelastic medium, to predict the resulting surface displacements. The afterslip model is purely kinematic and describes the slip distribution required on a downward continuation of the fault. In both cases, the stresses are imposed over a wide area, but in a homogeneous Maxwell viscoelastic material, strain will be distributed throughout the region, whereas in the afterslip model, the strain response is localized onto a single fault plane.

In reality, the postseismic deformation is likely to be caused by a mechanism intermediate to or a combination of these end-members. Predictions based on rate- and state-friction on a discrete fault plane suggest that at depths below the base of the seismogenic layer, frictional planes move by steady-state creep rather than stick-slip motion (Blanpied *et al.* 1991), potentially leading to the development of wide shear zones. Approaching the problem from the other end-member, viscoelastic relaxation in a power-law rheology would effectively localize strain into the region of highest imposed stress (Freed & Bürgmann 2004).

In past studies, the pattern of vertical displacement, to which InSAR is particularly sensitive, has been used to distinguish between afterslip and viscoelastic relaxation (Pollitz *et al.* 2001). However, in this case, both models are capable of providing a satisfactory fit to both GPS horizontal velocities and InSAR range change data. Regardless of mechanism, the vertical displacement component of the InSAR measurements provides good constraints on the depth of the deformation source.

This study has not considered poroelastic rebound, despite the fact that it has been shown to have significant effects in previous studies (Jonsson *et al.* 2003; Arnadottir *et al.* 2005) but not in others (Barbot *et al.* 2008). Stress changes imposed by an earthquake can induce pore pressure gradients in surrounding rock, which causes fluid to flow until equilibrium is reached. While undoubtedly important in some cases, the effects would be expected to be restricted

both spatially and temporally (Freed *et al.* 2006a). Poroelastic rebound requires both the presence of fluid and an interconnected pore space, and is likely to be restricted to the upper crust and cause displacements only within a few kilometres of the fault. The fluids concerned are of sufficiently low viscosity that equilibrium would be reached within a few months. Since the observations presented here are at much greater distances and over longer time periods, poroelastic rebound is unlikely to have a significant effect.

### 8.2 Lithospheric rheology

With the exception of some areas of shallow afterslip or poroelastic rebound, the majority of the postseismic response to the 2002 DF earthquake during 2003–2004 occurred in the upper mantle. The stresses imposed by the earthquake are greatest at the base of the seismogenic zone and decrease with depth, so the larger response from the upper mantle relative to the lower crust must result from differences in rheological stratification rather than stress distribution. In other earthquakes, such as Manyi, Tibet (Ryder *et al.* 2007) and Izmit, Turkey, (Hearn *et al.* 2002), the lower crust has been the major zone of relaxation, while in other cases (Landers, Hector Mine, California) upper mantle deformation was found to be important (Pollitz *et al.* 2001; Freed & Bürgmann 2004; Freed *et al.* 2007). For the Denali case, it is necessary to explain the difference between the upper mantle and lower crust and also between the lower crust in Alaska and in other parts of the world.

A decrease in viscosity can be caused by either an increase in temperature or a change in composition. Due to the proximity of the subduction zone, high temperatures are expected in the central Alaskan mantle, and seismic attenuation studies (Stachnik *et al.* 2004) have shown that the temperatures are elevated to $\sim$1250 °C but are not as high as in other mantle wedges. By assuming a power-law rheology with laboratory-derived parameters for dry olivine, $Q = 515\,\mathrm{kJ\,mol^{-1}}$ (Freed *et al.* 2006a), elevating the temperature at a depth of 80 km from a 'normal' temperature of 1200–1500 K would correspond to a decrease in effective mantle viscosity of four orders of magnitude. Alternatively, changing the composition from dry olivine to wet olivine (Freed *et al.* 2006a), as might be expected if fluids are released from the subducted slab, decreases the effective viscosity by three orders of magnitude. Lower temperatures or dehydration might cause a higher viscosity in the lower crust. Lower crust of granulite (dehydrated) compositions has been suggested as a cause of lower-crustal seismicity in cratonic areas such as Northern India (Maggi *et al.* 2000), but the accreted terranes which make up central and southern Alaska are principally composed of magmatic arcs.

The expected horizontal deformation from the locked subduction zone in the south is close to orthogonal to the line-of-sight vector, and contributes little to the observed phase changes. However, vertical displacements across the interferogram from the locked subduction zone and from rebound caused by post-Little Ice Age ice loss could contribute as much as 2 cm to the LOS displacement (Larsen *et al.* 2005).

### 8.3 Geodetic observations of postseismic responses

In the case of the Denali earthquake, a dense profile of cGPS stations perpendicular to the fault rupture would have produced results equivalent to those presented in this InSAR study. Consequently, in regions with good funding and good access, where a dense network of cGPS stations can be deployed, this remains the most accurate method of observing postseismic deformation. However, in situations with poor access, where dense GPS networks are not feasible, InSAR provides a remote geodetic method capable of measuring postseismic deformation. Due to limitations of interferometric coherence, this study used a single track of data, and consequently only covered a small length of the rupture. For earthquakes of this magnitude, several tracks of data are required to fully utilize the ability of InSAR to map the pattern of ground displacements. Previous studies have shown the importance of far-field displacements in distinguishing between mechanisms of postseismic displacement, but current InSAR observations are limited by the trade-offs between orbital parameters and long-wavelength displacements. This highlights the importance of improving orbital accuracy for InSAR satellites.

## 9 CONCLUSIONS

We conclude that the dominant response to the stresses imposed on the lithosphere, by the 2002 DF earthquake occurred in the upper mantle (depths greater than 50 km), during the time period between 1.5 and 2.5 yr after the earthquake. The observed surface displacements can be modelled by relaxation of a Maxwell viscoelastic medium or afterslip on a discrete fault plane or a combination of both. The lack of response in the lower crust can be explained by a viscosity ratio between lower crust and upper mantle of 5 or greater. Asymmetry in profiles of displacement taken across the fault cannot be explained simply by the geometry of the fault and may be a result of heterogeneity in the rheological structure of the region.

## ACKNOWLEDGMENTS

This work was funded by the Natural Environmental Research Council (NERC) through the Centre for the Observation and Modelling of Earthquakes and Tectonics (COMET) via a studentship to JB. The GPS data collection and analysis, and salary for JF, were supported by NSF grants EAR-0328043 and EAR-0310410. JB was also supported by a Harkness Fellowship from the University of Cambridge. TJW is supported by a Royal Society Research Fellowship. All the data were provided by the Canadian Space Agency, via the Alaska Satellite Facility. We would like to thank Philip England, Freystein Sigmundsson, Gareth Funning, John Elliott and Michael Floyd for useful discussions and to Sigurjon Jonsson and one anonymous reviewers for their constructive comments. We are grateful to Fred Pollitz for the use of the VISCO1D code.

## REFERENCES

Armstrong, M., 1998. *Basic Linear Geostatistics,* Springer, New York.

Arnadottir, T., Jonsson, S., Pollitz, F., Jiang, W. & Feigl, K., 2005. Postseismic deformation following the June 2000 Earthquake sequence in the south Iceland, *J. geophys. Res.,* **110,** doi:10.1029/2005JB003701.

Barbot, S., Hamiel, Y. & Fialko, Y., 2008. Space geodetic investigation of the coseismic and postseismic deformation due to the 2003 $M_w$ 7.2 Altai Earthquake: implications for the local lithospheric rheology, *J. geophys. Res. (Solid Earth),* **113,** doi:10.1029/2007JB005063.

Biggs, J., Bergman, E., Emmerson, B., Funning, G., Jackson, J., Parsons, B. & Wright, T., 2006. Fault identification for buried strike-slip earthquakes using InSAR: the 1994 and 2004 Al Hoceima, Morocco, earthquakes, *Geophys. J. Int.,* **166,** 1347–1362.

Biggs, J., Wright, T., Lu, Z. & Parsons, B., 2007. Multi-interferogram method for measuring interseismic deformation: Denali Fault Alaska, *Geophys. J. Int.,* **170,** 1165–1179.

Blanpied, M.L., Lockner, D.A. & Byerlee, J.D., 1991. Fault stability inferred from granite sliding experiments at hydrothermal conditions, *Geophys. Res. Lett.,* **18,** 609–612.

Brocher, T., Fuis, G., Lutter, W., Christensen, N.I. & Ratchkovski, N., 2004. Seismic velocity models for the Denali Fault Zone along the Richardson Highway, Alaska, *Bull. seism. Soc. Am.,* **96**(6B), S85–106.

Bürgmann, R. & Dresen, G., 2008. Rheology of the lower crust and upper mantle: evidence from rock mechanics, geodesy and field observations, *Ann. Rev. Earth. Planet. Sci.,* **36,** 531–567.

Bürgmann, R., Ergintav, S., Segall, P., Hearn, E., McClusky, S., Reilinger, R., Woith, H. & Zschau, J., 2002. Time-space variable afterslip on and deep below the Izmit Earthquake rupture, *Bull. seism. Soc. Am.,* **92,** 126–137.

Carver, G., Plafker, G., Metz, M., Cluff, L., Slemmons, B., Johnson, E., Roddick, J. & Sorensen, S., 2004. Surface rupture on the Denali Fault interpreted from tree damage during the 1912 Delta River $M_w$ 7.2-7.4 Earthquake: implications for the 2002 Denali Fault Earthquake slip distribution, *Bull. seism. Soc. Am.,* **94,** S58–S71.

Chen, C. & Zebker, H., 2000. Network approaches to two-dimensional phase unwrapping: intractability and two new algorithms, *J. Opt. Soc. Am.,* **17,** 401–414.

Dziewonski, A. & Anderson, D., 1981. Preliminary Reference Earth Model, *Phys. Earth planet. Int.,* **25,** 297–356.

Eberhart-Phillips, D. *et al.,* 2003. The 2002 Denali Fault Earthquake, Alaska: a large magnitude, slip-partitioned event, *Science,* **300,** 1113–1118.

Elliott, J., Freymueller, J. & Rabus, B., 2007. Coseismic deformation of the 2002 Denali Fault Earthquake: contributions from sar range offsets, *J. geophys. Res.,* **35,** doi:10.1029/2008GL033659.

Fialko, Y., 2004. Evidence of fluid-filled upper crust from observations of postseismic deformation due to the 1992 $M_w$7.3 Landers earthquake, *J. geophys. Res.,* **109,** 8401.

Fletcher, H., 2002. Crustal deformation in Alaska measured using the Global Positioning System, *PhD thesis*, University of Alaska, Fairbanks.

Freed, A.M. & Bürgmann, R., 2004. Evidence of power-law flow in the Mojave desert mantle, *Nature,* **430,** 548–551.

Freed, A., Bürgmann, R., Calais, E., Freymueller, J. & Hreinsdottir, S., 2006a. Implications of deformation following the 2002 Denali, Alaska, Earthquake for postseismic relaxation processes and lithospheric rheology, *J. geophys. Res.,* **111,** doi:10.1029/2005JB003894.

Freed, A., Bürgmann, R., Calais, E. & Freymueller, J., 2006b. Stress-dependent power-law flow in the upper mantle following the 2002 Denali, Alaska, earthquake, *Earth planet. Sci. Lett.,* **252,** doi:10.1016/j.epsl.2006.10.011.

Freed, A.M., Bürgmann, R. & Herring, T., 2007. Far-reaching transient motions after Mojave Earthquakes require broad mantle flow beneath a strong crust, *Geophys. Res. Lett.,* **34,** doi:10.1029/2007GL030959.

Freymueller, J.T., Cohen, S. & Fletcher, H., 2000. Spatial variations in present-day deformation, kenai peninsula, alaska, and their implications, *J. geophys. Res.,* **105,** 8079–8101.

Funning, G., Barke, R., Lamb, S.H., Minaya, E., Parsons, B. & Wright, T., 2005. The 1998 Aiquile, Bolivia Earthquake: a seismically active fault revealed with InSAR, *Earth planet. Sci. Lett.,* **232,** 39–49.

Goldstein, R. & Werner, C., 1998. Radar interferogram filtering for geophysical applications, *Geophys. Res. Lett.,* **25**(21), 4035–4038.

Gourmelen, N. & Amelung, F., 2005. Postseismic Mantle Relaxation in the Central Nevada Seismic Belt, *Science,* **310,** 1473–1476.

Govers, R., 1993. Dynamics of lithospheric extension; a modeling study, *PhD thesis*, University of Utrecht, Utrecht, Netherlands.

Hearn, E., Bürgmannn, R. & Reilinger, R., 2002. Dynamics of Izmit Earthquake postseismic deformation and loading of the Duzce Earthquake hypocenter, *Bull. seism. Soc. Am.,* **92,** 172–193.

Hreinsdottir, S., Freymueller, J., Bürgmann, R. & Mitchell, J., 2006. Coseismic deformation of the 2002 Denali Fault Earthquake: insights from GPS measurements, *J. geophys. Res.,* **111,** doi:10.1029/2005JB003676.

Jacobs, A., Sandwell, D., Fialko, Y. & Sichoix, L., 1999. The 1999 ($M_w$ 7.1) Hector Mine, California, Earthquake; near-field postseismic deformation from ERS interferometry, *Bull. seism. Soc. Am.,* **92,** 1433–1442.

Johnson, K., Burgman, R. & Freymueller, J., 2008. Coupled afterslip and viscoelastic flow following the 2002 Denali Fault, Alaska Earthquake, *Geophys. J. Int.*, in press.

Jonsson, S., Pedersen, R., Segall, P. & Bjornsson, G., 2003. Post-Earthquake ground movements correlated to pore-pressure transients, *Nature,* **424,** 179–183.

Kenner, S. & Segall, P., 2000. Postseismic deformation following the 1906 San Francisco Earthquake, *J. geophys. Res.,* **105,** 13 195–13 210.

Larsen, C., Motyka, R., Freymueller, J., Echelmeyer, K. & Ivins, E., 2005. Rapid viscoelastic uplift in southeast Alaska caused by post-Little Ice Age glacial retreat, *Earth planet. Sci. Lett.,* **237,** 548–560.

Maggi, A., Jackson, J., McKenzie, D. & Priestley, K., 2000. Earthquake focal depths, effective elastic thickness and the strength of the continental lithosphere, *Geology,* **28,** 495–498.

Matmon, A., Schwartz, D., Haeussler, P., Finkel, R., Lienkaemper, J., Stenner, H. & Dawson, T., 2006. Denali Fault slip rates and Holocene-late Pleistocene kinematics of central Alaska, *Geology,* **34,** 645–648.

Melosh, H.J. & Raefsky, A., 1980. The dynamical origin of subduction zone topography, *Geophys. J. R. astr. Soc.,* **60,** 333–354.

Melosh, H.J. & Raefsky, A., 1981. A simple and efficient method for introducing faults into finite element computations, *Bull. seism. Soc. Am.,* **71,** 1391–1400.

Parsons, B., Wright, T.J., Rowe, P., Andrews, J., Jackson, J., Walker, R., Khatib, M. & Talebian, M., 2006. The 1994 Sefiadbeh (eastern Iran) earthquakes revisited: new evidence from satellite radar interferometry and carbonate dating about the growth of an active fold above a blind thrust fault, *Geophys. J. Int.,* **164,** 202–217.

Plafker, G., Gilpin, L. & Lahr, J., 1994. Neotectonic Map of Alaska, in *The Geology of North America,* eds Plafker, G. & Berg, H.C., Geol. Soc. Am., Boulder, CO.

Pollitz, F., 1992. Postseismic relaxation theory on a spherical Earth, *Bull. seism. Soc. Am.,* **82,** 422–453.

Pollitz, F., 2005. Transient rheology of the upper mantle beneath central Alaska inferred from the crustal velocity field following the 2002 Denali Earthquake, *J. geophys. Res.,* **110,** doi:10.1029/2005JB003672.

Pollitz, F., Peltzer, G. & Bürgmann, R., 2000. Mobility of continental mantle: evidence from postseismic geodetic observations following the 1992 Landers Earthquake, *J. geophys. Res.,* **105,** 8035–8054.

Pollitz, F., Wicks, C. & Thatcher, W., 2001. Mantle flow between a continental strike-slip fault: postseismic deformation after the 1999 Hector Mine Earthquake, *Science,* **293,** 1814–1818.

Ratchkovski, N., Weimer, S. & Hansen, R., 2004. Seismotectonics of the Central Denali Fault, Alaska and the 2002 Denali Fault Earthquake Sequence, *Bull. seism. Soc. Am.,* **96**(6B), S85–S106.

Ryder, I., Parsons, B., Wright, T.J. & Funning, G.J., 2007. Post-seismic motion following the 1997 Manyi (Tibet) Earthquake: InSAR observations and modelling, *Geophys. J. Int.,* **169,** 1009–1027.

Schmalzle, G., Dixon, T., Malservisi, R. & Govers, R., 2006. Strain accumulation across the Carrizo segment of the San Andreas Fault, California: impact of laterally varying crustal properties, *J. geophys. Res.,* **111,** doi:10.1029/2005JB003843.

Stachnik, J., Abers, G. & Christensen, D., 2004. Seismic attenuation and mantle wedge temperatures in the Alaska subduction zone, *J. geophys. Res.,* **109,** doi:10.1029/2004JB003018.

Veenstra, E., Christensen, D., Abers, G. & Ferris, A., 2006. Crustal thickness variation in south-central alaska, *Geology,* **34,** 781–784.

Wright, T., Lu, Z. & Wicks, C., 2003. Source model for the $M_w$6.7 23 October 2002 Nenana Mountain Earthquake (Alaska) from InSAR, *Geophys. Res. Lett.,* **30,** doi:10.1029/2003GL018014.

Wright, T., Lu, Z. & Wicks, C., 2004. Constraining the slip distribution and fault geometry of the Mw7.9, 2 November 2002, Denali Fault Earthquake with interferometric synthetic aperture radar and global positioning system data, *Bull. seism. Soc. Am.,* **94**(6B), S175–S189.

## SUPPORTING INFORMATION

Additional Supporting Information may be found in the online version of the article.

**Figure S1.** Baseline-time plot showing interferograms used in this study. Blue lines represent interferograms used in the 2003–2004 time period; green lines for the 2004-2005 period and black lines for those interferograms used in both.

**Figure S2.** Histograms showing the distribution of orbital parameters for the Radarsat interferograms. A least-squares inversion is used to find the best-fitting function of the form $z = ax + by + cxy + dx2 + ey2$ to the geocoded interferograms. The random distribution of parameters is consistent with the assumption that the quadratic function fits the orbital rather than deformation component of the interferogram.

**Figure S3.** Comparison between InSAR and GPS estimates of vertical motion including error bars.

**Table S1.** Radar data collected by the Canadian Radarsat-1 satellite during the period 2003-2005.

Please note: Wiley-Blackwell are is not responsible for the content or functionality of any supporting materials supplied by the authors. Any queries (other than missing material) should be directed to the corresponding author for the article.